



Snow water equivalent retrieved from X- and dual Ku-band scatterometer measurements at Sodankylä using the Markov Chain Monte Carlo method

Jinmei Pan¹, Michael Durand², Juha Lemmetyinen³, Desheng Liu⁴, Jiancheng Shi⁵

5 ¹State Key Laboratory of Remote Sensing Science, Aerospace Information Research Institute, Chinese Academy of Sciences, Beijing 100101, China

²School of Earth Science and Byrd Polar Research Center, The Ohio State University, Columbus, OH 43210, USA

³Finnish Meteorological Institute, Helsinki FI-00101, Finland

⁴Department of Geography, The Ohio State University, Columbus, OH 43210, USA

10 ⁵National Space Science Center, Chinese Academy of Sciences, Beijing 100190, China

Correspondence to: Jinmei Pan (jinmei.pan@gmail.com)

Abstract. Radar at high frequency is a promising technique for fine-resolution snow water equivalent (SWE) mapping. In this paper, we extend the Bayesian-based Algorithm for SWE Estimation (BASE) from passive to active microwave (AM) application and test it using ground-based backscattering measurements at three frequencies (X- and dual Ku-bands, 10.2, 13.3 and 16.7 GHz), VV polarization
15 obtained at 50° incidence angle from the Nordic Snow Radar Experiment (NoSREx) in Sodankylä, Finland. We assume only an uninformative prior for snow microstructure, in contrast with an accurate prior required in previous studies. Starting from a biased SWE prior from land surface model simulation, two-layer snow state variables and single-layer soil variables are iterated until their posterior distribution could stably reproduce the observed microwave signals. The observation model is the Microwave Emission Model of Layered Snowpacks 3 and Active (MEMLS3&a). Results show that BASE-AM achieved a RMSE of ~10 cm for snow depth (SD) and less than 30
20 mm for SWE, compared with the RMSE of ~20 cm SD and ~50 mm SWE from priors. Retrieval errors are significantly larger when BASE-AM is run using a single snow layer. The results support the potential of X- and Ku-band radar for SWE retrieval and shows that providing a fully-unbiased snow microstructure prior is not the only promise to obtain accurate SWE retrievals.

1 Introduction

Every year, snow and ice covers about 50% of the land surface in the Northern Hemisphere (Brown & Robinson, 2011),
25 reflects back up to 80% of the solar radiation, cools the Earth's surface (Flanner et al., 2011), and provides water supplies for about 1/6 of the world's population (Barnett et al., 2005). The estimation of snow water equivalent (SWE), which describes the equivalent depth of liquid water when snow completely melts (Takala et al., 2011), is of critical importance for hydraulic and hydrological applications (Lettenmaier et al., 2015). However, current observation-based estimates of global snow lack precision and spatial resolution needed to capture global processes (Mortimer et al., 2020); snow is the most poorly
30 measured component of the global water cycle (Durand et al., 2021).



Active microwave radar at the X- and Ku-bands shows great promise for high resolution snow depth and SWE mapping (Rott et al., 2012; Tsang et al., 2022). This technique is based on detecting changes in volume scattering from the snow medium, and thus builds from the heritage from passive microwave remote sensing (Tsang et al., 2022). Active microwave remote sensing can achieve far higher spatial resolution than passive microwave via synthetic aperture radar (SAR) processing. The existence of snow on the ground and its volume scattering generally increases the backscattered radar signal as compared to bare soil. Multiple satellite mission proposals have proposed to use this technique, but none have so far been selected for space-borne operations. The Snow and Cold Lands Processes (SCLP) mission proposed to NASA, the Cold Regions Hydrology High-resolution Observatory (CoReH₂O) proposed to ESA, and The Water Cycle Observation Mission (WCOM) proposed in China were all to have been dual-frequency radars operating at X- and Ku- bands (Cline et al., 2007; Rott et al., 2012; Shi et al., 2014). The Canadian Space Agency (CSA) is currently considering a concept study for a satellite radar mission for terrestrial snow mass, proposing a dual Ku-band scatterometer (Derksen et al., 2021; Tsang et al., 2022). The maturity of the algorithms to retrieve SWE from radar signal has grown significantly as described by Tsang et al. (2022), but algorithm challenges remain. New work on Ku- and X- retrievals is continuing, for example in the NASA SnowEx experiments featuring the SWESARR instrument (Rincon et al., 2020).

Algorithm development for Ku- and X- SAR retrievals is of vital importance. The radar backscatter from snow is sensitive to SWE but is complicated by confounding factors including snow microstructure, the backscatter from the substrate beneath snow, and forest cover (Tsang et al., 2022). Recent advances have begun to resolve the substrate issue, specifically by subtracting the contribution of the rough surface scattering at the snow-soil interface (e.g. Zhu et al., 2018) and using passive microwave measurements (Zhu et al., 2021). Forests pose an important limitation on the applicability of the technique, and recent studies have helped refine estimates of forest conditions under which SWE may be estimated (e.g. Macelloni et al., 2017; Lemmetyinen et al., 2022). In this paper, we focus on retrieval issues posed by snow microstructure.

The complexities of retrieving SWE from radar measurements derive from fundamentals of snow physics and electromagnetic physics. Radar backscatter is highly sensitive to snow microstructure, commonly characterized by the size of the individual snow crystals (e.g. Xu et al., 2010; King et al., 2018; Rutter et al., 2019). Because grain shape is highly irregular and exhibits significant spatiotemporal variability, and because grains are oftentimes well-bonded within snowpack, we often refer to “snow microstructure” or to the microstructure correlation length rather than grain size (Picard et al., 2023). Specifically, we estimate the exponential correlation length (Mätzler, 2002) of the snow microstructure in this study. Exponential correlation length can be thought of as the length scale describing the ice-air medium, i.e. the length at which one would expect the medium to change from ice to air. High values of correlation length generally correspond to high values of grain size; Pan et al. (2017) explored the relationship between grain size and correlation length for the NoSREx dataset. Radar backscatter is quite sensitive to snow microstructure, and the dependence is highly non-linear. These complexities have led algorithm developers to introduce a priori information on grain size to help constrain the retrieval problem (Tsang et al., 2022), which in turn makes the retrieved SWE accuracy dependent on the unbiasedness of the prior grain size, at least to some extent. The CoReH₂O mission specified that an effective grain radius must be known a priori to



65 within 15% precision to enable SWE retrieval, a daunting requirement indeed. Rutter et al. (2019) similarly found in context
of a sensitivity experiment that depth hoar equivalent grain size must be specified to within 5-10% precision in order to
achieve a ± 30 mm SWE accuracy requirement (IGOS, 2007). Despite recent advances, capabilities to predict grain size still
fall below the required precision, creating a dilemma for retrieval algorithms. As described by Tsang et al. (2022), the
70 approach of Cui et al. (2016) and Zhu et al. (2018; 2021) reframes the need for prior information. Furthermore, Merkouriadi
et al. (2021) indicated that applying physical model to generate priors of grain size is not straightforward, as biased SWE
estimates in physical models lead to large biases in the modelled microstructure, which in turn propagate as an increase of
bias in a potential microwave retrieval using these as priors.

While past work focused on an error propagation approach to infer the required precision for an equivalent grain size,
retrieval algorithms that explicitly statistically model each unknown term in the retrieval problem have not been explored in
75 the literature. Here, we extended the Bayesian-based Algorithm for SWE Estimation (BASE) (Pan et al., 2017) to active
microwave (AM) application. Unlike a simple steepest descent algorithm or Newton's method, a Markov Chain Monte Carlo
(MCMC) method is used in BASE-AM, providing posterior distributions of several variables at the same time from
observations and prior distributions, without any assumption of linear error propagation. We test BASE-AM SWE retrieval
using ground-based radar measurements from the Nordic Snow Radar Experiment (NoSREx; Lemmetyinen et al., 2016). We
80 use the Microwave Emission Model of Layered Snowpacks 3 and Active (MEMLS3&a) (Proksch et al., 2015) as the
observation model, and consider a two-layer snow structure, composed of a surface layer and a depth hoar layer. We
iteratively update the snow layer thickness, snow exponential correlation length, snow density, snow temperature, soil
temperature, soil roughness, total soil water content, and one semi-empirical model variable in MEMLS 3&a to build
MCMC chains. The exponential correlation length is the snow microstructure parameter specifically used in MEMLS 3&a.
85 We deliberately choose a biased SWE prior from land surface model simulations compared with the in-situ observations, and
thus implicitly test whether radar data can overcome such biases. Acknowledging the challenge of obtaining appropriate
grain size priors, we choose a fixed and nearly uninformative prior (0.18 ± 0.09 mm for exponential correlation length
(Mätzler, 2002).

If the algorithm successfully estimates SWE, then the two-layer approach with a biased prior on SWE and an uninformative
90 prior for grain size contains adequate information to estimate SWE, thus providing a new perspective on the need for prior
information outlined by Rott et al. (2012) and Rutter et al (2019). If the algorithm is unsuccessful, we'll have found that a
precise prior for grain size are required, in agreement with previous literature.

2 Data

From 2009 to 2013, continuous snow radar experiments were conducted at the Intensive Observation Area (IOA) (67.362°N ,
95 26.633°E) located in the Finnish Meteorological Institute Arctic Research Centre (FMI-ARC) in Sodankylä, Finland, during
the NoSREx campaign (Lemmetyinen et al., 2016). The IOA is located in a clearing of a typical Scots pine (*Pinus sylvestris*)



boreal forest on mineral soil. A The X- and dual-Ka band scatterometer SnowScat of the European Space Agency (ESA) was installed on a tower at the height of 9.6-m to observe the undisturbed, natural snowpack at several incidence and azimuth angles. Manufactured by GAMMA Remote Sensing, SnowScat, is a stepped frequency, four-polarization (VV, HH, 100 VH and HV polarizations) radar operating from 1-18 GHz. The single-look complex measurements were sampled to 1 GHz bands with centre frequencies of 10.2, 13.3 and 16.7 GHz. SnowScat provides an internal calibration loop for tracking stability of the transmitted signal. Stability was further verified to be within the goal of +/- 1 dB by observing an aluminum sphere target before and after each acquisition scan.

The goal of NoSREx was to observe the backscattering coefficient (σ_0) from before snow onset until after snow 105 disappearance at regular intervals. For the first season in 2009-2010, a three-hour measurement interval was used. This was extended to four hours for later seasons (2010-2011, 2011-2012, 2012-2013). The seasons are referred to as Intensive Observation Periods (IOPs) 1-4 in this paper. The acquisition scan consisted of 17 independent look directions in azimuth at four elevation angles, corresponding to ground incidence angles of 30, 40, 50 and 60°. Our retrieval used only the VV polarization at a fixed 50° incidence angle. The applied backscattering values represent an average over the 17 independent 110 looks.

Concurrently, snowpits were excavated near the SnowScat, twice per week for the first season and weekly for the following seasons. Snow depth, snow stratigraphy and geometric grain size of each snow layer were measured; the snow temperature and snow density were measured by 10-cm and 5-cm steps, respectively. There were also several automatic sensors installed at IOA to provide additional information. Continuous SWE measurements were available from the Gamma Snow Instrument 115 (GWI), although it tends to be contaminated by high-frequency noise at short time scales. Soil temperature and soil liquid water content were measured by the Delta-T Devices ML2x sensor at 2-cm in four IOPs, and by the Decagon 5TM sensors at 5, 10, 20, 40 and 80 cm in IOP3 and 4. Soil at the IOA has a texture of 70% sand, 29% silt and 1% clay, and a bulk density of 1300 kg/m³. Mineral soils are overlain by a thin organic layer of 2-5 cm of lichen and heather.

Fig.1 shows the measured backscattering coefficients at VV-pol. at 50° incidence angle, with the measured SWE, geometric 120 grain size (D_g), snow density and soil liquid water content. The D_g and snow density presented here are mass-weighted average values along the snow profile. From the figure, there is not a simple relationship between volume scattering and maximum SWE among the four IOPs. For example, IOP2 has the maximum backscatter values at 16.7 GHz and the maximum ratio of the 16.7 and 10.2 GHz channels; however, the maximum SWE for IOP2 is the smallest of the four years. At the same time, IOP2 has a relatively high geometric snow grain size (D_g), larger than IOP3 and 4 and comparable to IOP1. 125 It agrees with the physical theory that a shallower snow tends to have a larger snow grain size, because of a stronger temperature gradient inside the snow (Jordan, 1991). Thus, among the four IOPs, the influence of snow microstructure is higher than that of SWE. However, as shown in Fig.2, within each IOP, the backscattering ratio between 16.7 and 10.2 GHz increases with both snow depth (SD) and geometric snow grain size (D_g). During IOP1 and 4, the correlations between the backscattering ratio and SWE in (a) can be classified into two groups; this is because of a stronger snow grain growth speed 130 at the very early snow season compared to the mid-snow season.



Concerning other variables, Fig.1 shows the IOPs with a higher maximum SWE tends to have a higher average snow density. It also agrees with the snow compaction theory according to snow process model (Jordan, 1991). The underlying soil was frozen for most of the snow season; however, it was unfrozen and had a large soil water content in the early and late snow season because of snowmelt. Fig.2(c)-(d) shows more details with respect to the measured backscattering coefficient at 10.2
135 GHz ($\sigma^{VV}_{0,10.2}$). Specifically, IOPs with a lower liquid water content or a higher average snow density tends to have higher $\sigma^{VV}_{0,10.2}$. The significantly different $\sigma_{0,10.2}$ between different IOPs indicates a requirement to estimate soil and snow parameters simultaneously.

140

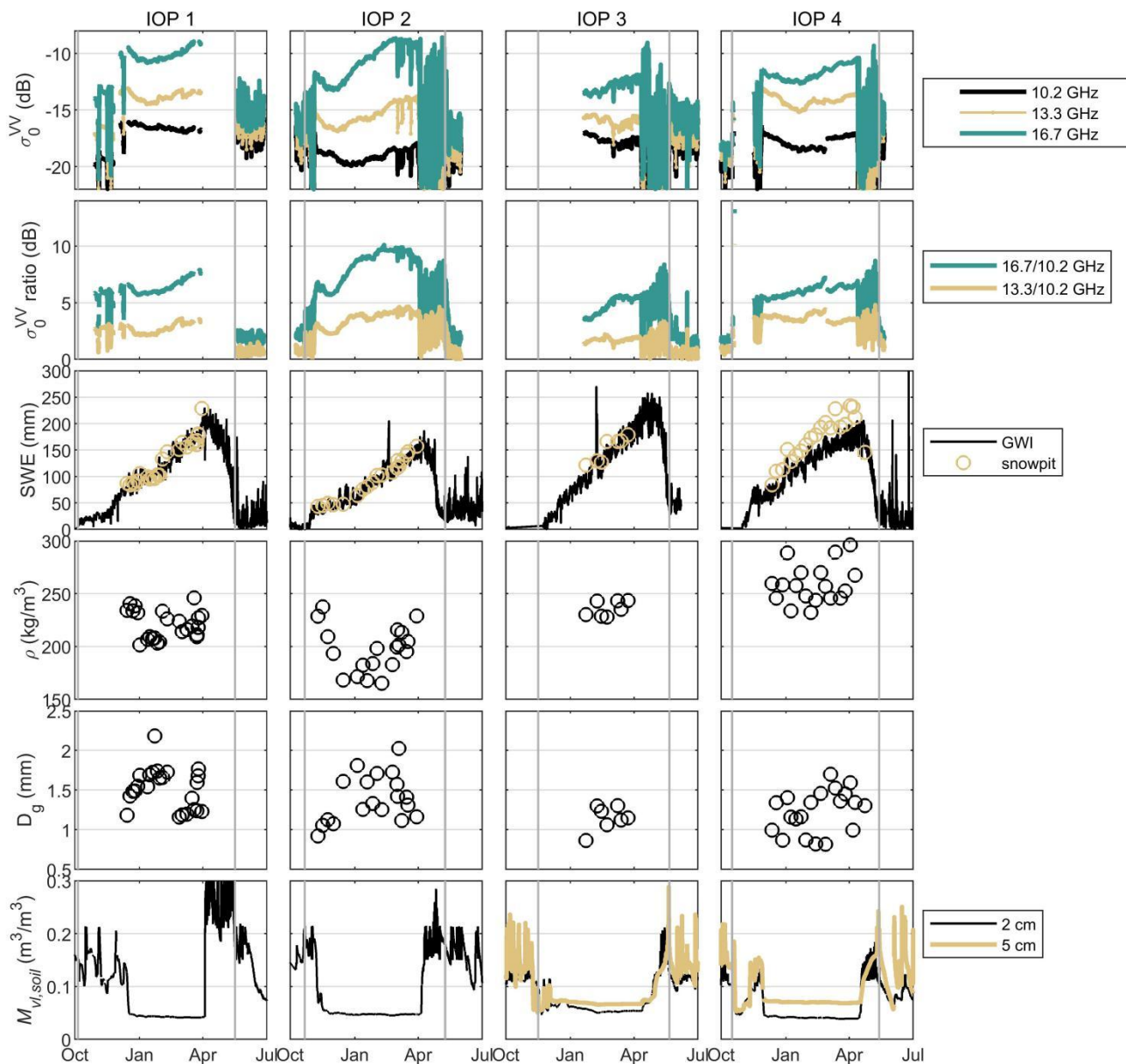


Figure 1: Measured backscattering coefficient at VV-pol. (σ^{VV}_0) and snow parameters in four IOPs in NoSREx in different columns. The first row shows σ^{VV}_0 at three frequencies at 50° incidence angle; the second row shows ratio of σ^{VV}_0 between two frequencies; the third row show the snow water equivalent (SWE); the fourth row shows the profile-average snow density weighted by snow mass (ρ); the fifth row shows the profile-average geometric grain size weighted by snow mass (D_g); the sixth row shows the measured liquid water content ($M_{vl,soil}$) by Delta-T Devices ML2x sensor (2 cm) and the Decagon 5TM sensors (5 cm). The circles are used for measurements from snowpits for SWE, ρ , and D_g . Grey vertical bars are used to indicate the onset and end of snow season, identified according to snow depth measurements.

145

150

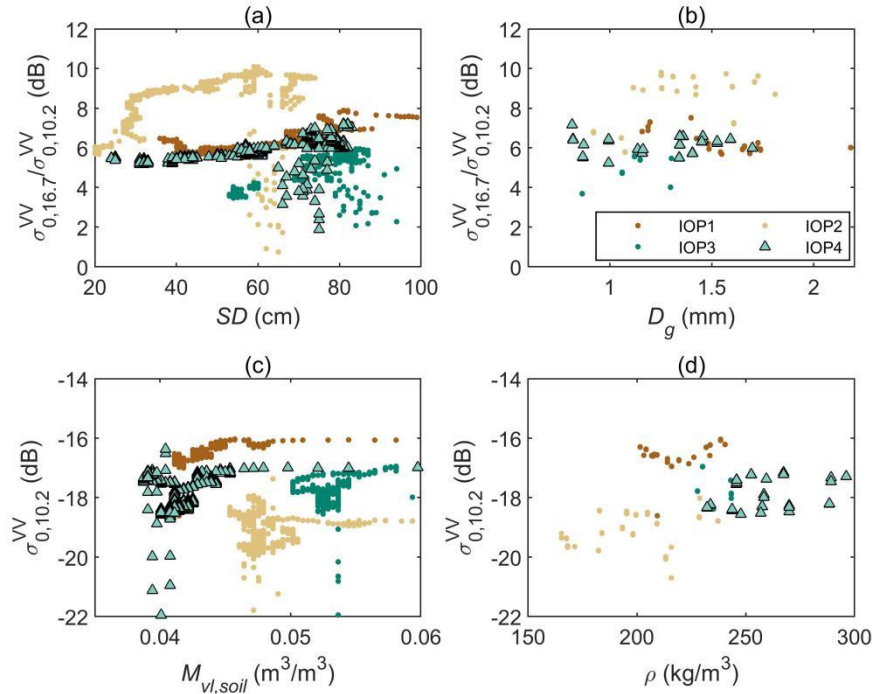


Figure 2: Relationships between measured ratio of σ^{VV}_0 between 16.7 and 10.2 GHz and snow depth (SD) (a) and geometric grain size (D_g) (b), respectively. Relationships between measured σ^{VV}_0 at 10.2 GHz in frozen soil period with soil liquid water content (c) and snow density (d), respectively. All the data presented here require a soil temperature at 2 cm < 0 °C.

155 3 Method

3.1 The Markov Chain Monte Carlo (MCMC) method

In this paper, we adapted the Bayesian-based Algorithm for SWE Estimation (BASE) used for inverting passive microwave radiometer measurements in Pan et al. (2017) to radar data. The Markov Chain Monte Carlo method (Gelman et al., 1995) is a numerical realization of the Bayes' theorem. Starting from a prior distribution of predicted variables, MCMC randomly searches within the minimal to maximum range of each variable and picks estimates that are both close to the prior and to the observations through the radiative transfer model. The likelihood ratio (R) is used to assess the relative proximity of two sets of SWE and soil parameters to the prior and the observations:

$$R = \frac{P_{obs}(M(x_1))P_{pr}(x_1)}{P(M(x_2))P_{pr}(x_2)} \quad (1)$$

where, x_1 is the first set of predicted variables, x_2 is the second set. $P_{pr}(x_1)$ and $P_{pr}(x_2)$ are the probability of x_1 and x_2 according to the prior distribution. M is the MEMLS3&a observation model, and $P_{obs}(M(x_1))$ and $P_{obs}(M(x_2))$ are the probability of model-simulated backscattering coefficients, $M(x_1)$ and $M(x_2)$, according to a normal distribution centered at



the observed backscattering coefficients, with a standard deviation of 0.5 dB at each frequency and zero covariance between different frequencies.

At each iteration, if the MCMC algorithm tries to change the value of an estimated variable from x_1 to x_2 , the likelihood ratio, R , is calculated. If R is larger than 1 or larger than a uniformly-distributed random threshold R_c between 0 and 1, the change will be accepted; otherwise, it will be rejected. The randomness in R_c is used to prevent local optimization. Finally, all the iterations will build a vector for each estimate variable, which is called the MCMC chain. The MCMC chain is the numerical realization of the posterior distribution, from which we can calculate the final retrieval results and their uncertainties using the mean and the standard deviation.

MCMC applied here differs with Pan et al. (2017) in the following aspects:

- 1) The observations and observation model were changed from passive to active (radiometer brightness temperature to radar backscatter).
- 2) The prior distributions were changed from lognormal distributions to normal distributions, because lognormal-distributed prior leads to lognormal-distributed posterior distribution, which has a skewness that is challenging to interpret.
- 3) Snow layer thicknesses were independently estimated in Pan et al. (2017); in this study, we estimate bottom-layer thickness and a relative thickness of the surface layer compared to the bottom layer. This was done because we found that the penetration ability of radar at these frequencies have largely reduced the sensitivity to volume scattering from the surface snow layers of small grain sizes. The use of layer thickness ratio predetermined the existence of the surface layer, and it was assumed to follow a normal distribution of 1 ± 0.2 (a ratio of 1 indicates that the two layers have the same thickness). In addition, we constrained the density and temperature of the surface layer to be lower than the bottom layer. The constraints were realized by dynamically using the bottom-layer density and temperature to be the upper limits of those in the surface layer at each iteration.

We refer to the algorithm described above as BASE-AM (Active Microwave). As in Pan et al. (2017), the algorithm runs 20,000 iterations, with a burn-in period of 5,000. The burn-in period was used to allow the variables to walk from the initial status to the status that can stably reproduce the observation. The final retrieval results are averaged from the MCMC estimates between the 5,001 to 20,000 iterations.

Table 1 lists all variables estimated in MCMC algorithm and their priors utilized in this paper. The snow and soil priors are close to the generic prior used in Pan et al. (2017) for Sodankylä. However, the standard deviations of priors were cut half compared to Pan et al. (2017), because the boundaries of normal distributions are less constrained than lognormal distributions. The SWE prior was a multiple-year average of monthly-mean SWE from global 2-degree VIC model simulations (Nijssen et al., 2001). The snow density and snow temperature priors were from the taiga snow type in Sturm's snow classes (Sturm et al., 1995; 2000). The prior for snow exponential correlation length was uninformative: 0.18 ± 0.09 mm. The soil temperature prior was set the same as snow temperature prior. The prior for total soil water content was set as $8 \pm 4\%$ vol. The soil roughness prior was set as 1 ± 0.5 cm.



Table 1. Summary of priors and boundaries for each estimate variables

Parameter		Mean of prior	Standard deviation (s.t.d.) of prior	Minimal value allowed in MCMC	Maximum value allowed in MCMC	Other constraints
Snow depth	Thickness of the bottom layer	Calculated from priors for snow density and SWE from VIC simulations*	Calculated from s.t.d. of snow density and SWE from VIC simulations*	1 mm	10 m	No
	Relative thickness of surface layer compared to bottom layer	1	0.2	0.001	1	No
Snow density		217 kg/m ³	56 kg/m ³	50 kg/m ³	917 kg/m ³	Surface density ≤ bottom density
Exponential correlation length (p_{ex})		0.18 mm	0.09 mm	0.001 mm	5 mm	No
Snow temperature		-10 °C	5 °C	-30 °C	0 °C	Surface temperature ≤ bottom temperature
Soil temperature		-10 °C	5 °C	-30 °C	0 °C	No
Soil RMSE-height		1 mm	0.5 mm	0 mm	10 cm	No
Total soil water content ($M_{v,soil}$)		8%	4%	0%	100%	No
MEMLS3&a polarization splitting parameter (Q)		0.1	0.01	0.08	0.12	No

* the mean of SWE prior is VIC-simulated average value of monthly mean SWE, and s.t.d. of prior is half of the mean.

3.2 The MEMLS3&a snow backscattering model

The forward observation model to calculate the snow backscattering was the Microwave Emission Model of Layered Snowpacks 3 and Active (MEMLS 3&a) (Proksch et al., 2015). MEMLS3&a for active backscattering simulation is a semi-empirical model that converts passive microwave reflectivity of the snowpack to backscattering. It assumes the distribution of the diffuse part of the bistatic scattering coefficient is Lambertian. In this model, first the snow reflectivity calculated by passive MEMLS (r) is separated into a specular part (r_s) and a diffuse part (r_d). r_s is calculated from the specular part of soil reflectivity, attenuated by snow absorption and snow scattering layer by layer (see equation (14) in Proksch et al. (2015)). Afterward, $r_d = r - r_s$, and r_d is converted to the diffuse part of the backscattering coefficient (σ_d^0) based on the Lambertian assumption as:

$$\sigma_d^0 = 4r_d\mu_0^2 \quad (2)$$

where. μ_0 is $\cos(\theta_0)$, and θ_0 is the incidence angle.

After σ_d^0 is calculated, the specular part of backscattering coefficient (σ_s^0) is calculated using Geometrical-Optics (GO) theory; σ_s^0 is assumed the same for co-polarizations and zero for cross-polarizations, and was calculate from the specular part of



reflectivity (r_s) and a roughness parameter (m^2) (see equation (9) in Proksch et al. (2015)). Finally, the total snow backscattering coefficient is calculated as:

$$\sigma_{pp'}^0 = \begin{cases} (1-Q)\sigma_{d,v}^0 + \sigma_s^0 & p = p' = v \\ (1-Q)\sigma_{d,h}^0 + \sigma_s^0 & p = p' = h \\ Q(\sigma_{d,v}^0 + \sigma_{d,h}^0)/2 & p \cong p' \end{cases} \quad (3)$$

In MEMLS3&a, there are two empirical parameters. The first one is Q , utilized to split $\sigma_{d,v}^0$ into co-polarizations and cross-polarizations. Our forward simulation test based on snowpit measurements suggested a Q between 0.8 and 1.2 at Sodankylä. Therefore, the prior for Q was set as 0.1 ± 0.01 in Table 1. The second empirical parameter in MEMLS3&a is the roughness parameter in GO, which is the mean-squared slope (m^2). We fixed m^2 to a value of 0.01 according to simulations, because we found it only influences backscattering at small incidence angles ($< 30^\circ$).

3.3 Soil models

MEMLS3&a requires the total and specular part of soil reflectivity, instead of soil backscattering. We utilized the QHN model with frequency-independent parameters (QHNfi) developed in Montpetit et al. (2015) to calculate the total soil surface reflectivity. The specular part (Γ_p^s) of the soil reflectivity is calculated as (Mo et al., 1987; Wegmüller and Matzler, 1999):

$$\Gamma_p^s = [(1 - Q_s)\Gamma_p^* + Q_s\Gamma_q^*] \exp(-4k^2\sigma^2 \cos^2\theta_1) \quad (4)$$

where, Γ_p^* and Γ_q^* are the Fresnel reflectivities. k is the wave number. σ is the soil roughness (RMS-height of soil surface). θ_1 is the local incidence angle at the snow-soil boundary. Q_s is the polarization mixing parameter for soil surface scattering, which is set the same as in QHNfi.

The soil dielectric constants were calculated using a revised Generalized Refractive Mixing Dielectric Model (GRMDM) (Mironov et al., 2004) adapted for frozen soil. The frozen soil is considered as a mixture of dry solids, bound water, transient water and ice as in Mironov et al. (2017). The model utilized the same bound water content as in Mironov et al. (2004), whereas it fitted temperature dependent bound water dielectric constants and other important variables using data from a soil experiment conducted using a vector network analyzer at Beijing Normal University; see Appendix I.

4 Results

4.1 MCMC performance for active SWE retrieval

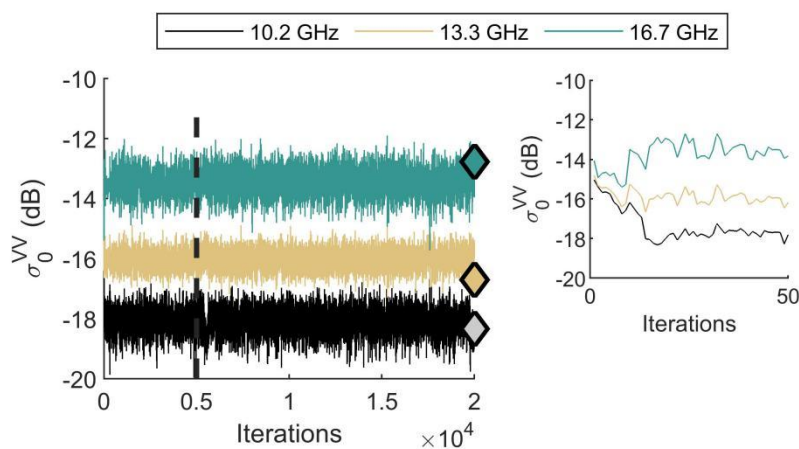
Fig. 3-5 uses the snowpit measured on March 13th, 2012 during IOP 3 (hereafter we call it Pit 49) as an example to show how MCMC works. Fig. 3 shows the simulated backscattering coefficient at each iteration, whereas Fig. 4 and 5 shows the variations of all estimated variables at each iterations.



Fig. 3 shows that the simulated backscattering coefficients at each point in the chain (after burn in) are close to the observations, which is one of the key points of MCMC-based retrieval. The mean bias is 0.23, 0.68 and -0.66 dB at 10.2, 13.3 and 16.7 GHz, respectively, after the burn-in period. The enlarged plot on right shows the influence of initial values of variables on the first 20 iterations.

Fig 4 shows the MCMC chains (left) and the posterior distributions (right) of the snow variables. The posterior distributions of layer thickness (first row) have lower uncertainty than the priors, and the mean is different than the prior. For the estimation of exponential correlation length (p_{ex}) (second row), the BASE-AM algorithm predicts a smaller surface- p_{ex} and a larger bottom-layer p_{ex} , although the relative relationship between two layers for p_{ex} was not constrained. As shown in the width of the posterior distribution, the uncertainty of surface layer p_{ex} is larger than bottom-layer p_{ex} . In the third row, the surface-layer snow density is smaller than bottom-layer density. However, this is simply a realization of our constraint on the relative relationship between snow densities. In the fourth row, the backscattering coefficient is not sensitive to snow temperature, so the posterior distributions of snow temperature highly overlap with the priors. The surface-layer snow temperature was constrained to be lower than the bottom layer in MCMC iterations, and it was realized as shown here.

Fig 5 shows the MCMC chains (left) and the posterior distributions (right) of the soil and model variables. The first row shows that the backscattering coefficient is not sensitive to soil temperature or to the model variable, Q , in the fourth row: their posterior distributions follow the prior distributions. The second and third rows show that the algorithm gives a small value for total soil water content, whereas the soil roughness varies. This behavior is not identical among snowpits; the total soil water content can have greater variability than soil roughness. The backscattering coefficient at low frequency in this paper is limited, so the algorithm cannot stably estimate soil roughness and soil moisture variables at the same time. This is discussed in detail in Section 5.1.



265 **Figure 3: MCMC chain of simulated backscattering coefficients (lines) compared with the measured backscattering coefficients (diamonds) for Pit 49. An enlarged plot for the first 50 iterations is added on the right.**

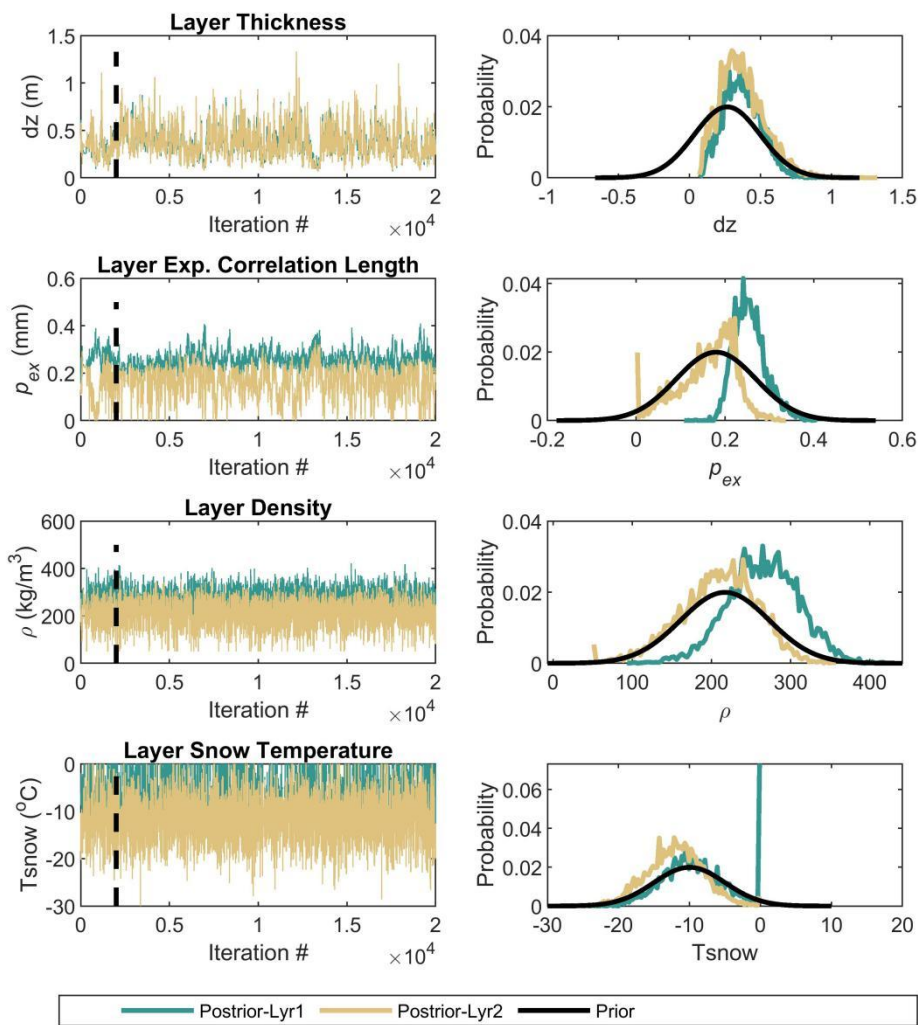
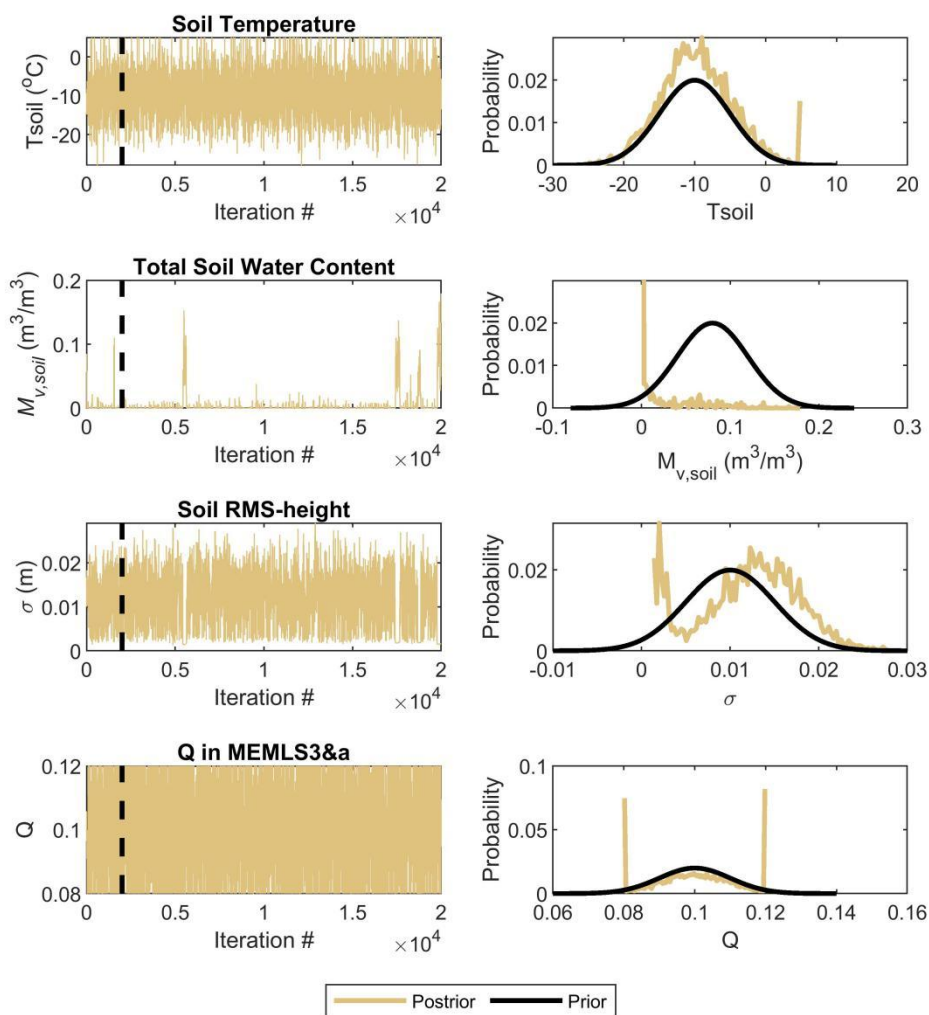


Figure 4: MCMC chain of layered snow properties (first column) and their posterior distributions compared with the prior distributions (second column) for Pit 49.



275

Figure 5: MCMC chain of other soil and model variables (first column) and their posterior distributions compared with the prior distributions (second column) for Pit 49.

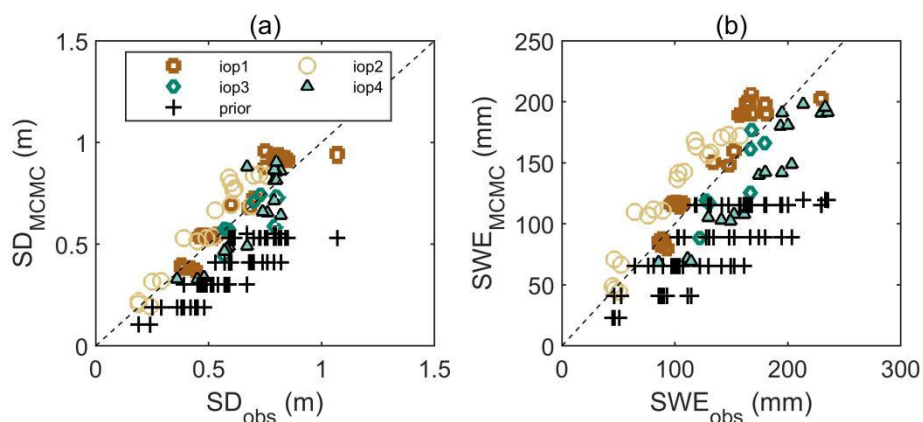
4.2 Estimation of snow depth and snow water equivalent

Fig. 6 shows the MCMC-estimated snow depth (SD) (a) and SWE (b), from the averages of MCMC chains after the burn-in period. The BASE-AM algorithm corrects the underestimation of VIC priors: the original biases for SWE are -49.6, -16.8, -54.5 and -87.9 mm for IOP 1, 2, 3, 4, respectively, whereas the biases are reduced to 12.3, 25.8, -15.3 and -34.8 mm for four IOPs after retrieval. Fig. 7 summarizes the root-mean-squared error (RMSE). On average, the BASE-AM algorithm reduces the posterior RMSE to about half of the prior. The SWE RMSE for all snowpits is within 30 mm, whereas the SD RMSE for

280

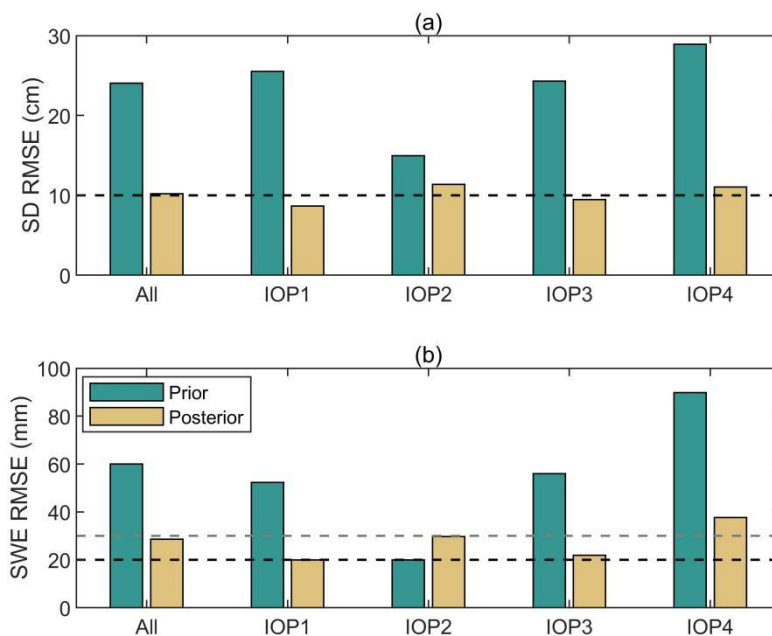


all snowpits is close to 10 cm. For IOP2, the posterior SWE RMSE is higher than prior RMSE, because of an overestimation of both SD and snow density.



285

Figure 6: BASE-AM estimated snow depth (SD) versus observed snow depth at Sodankylä (a), and BASE-AM estimated snow water equivalent (SWE) versus observed SWE (b).



290

Figure 7: Summary of root-mean-squared error (RMSE) for SD (a) and SWE (b) for different IOPs. The black dash lines are 10 cm RMSE for SD. The black and grey dash lines are 20 and 30 mm RMSE for SWE.



4.3 Estimation of snow microstructure

Fig. 8 shows a comparison between the MCMC-estimated exponential correlation length (p_{ex}), p_{ex} converted from the measured D_g using the conversion equation in Pan et al.(2017), as $p_{ex}=0.227+0.126*\log(D_g)$, and fitted p_{ex} from the use of MEMLS3&a to match the measured three-frequency backscattering coefficient for each snowpit. To calculate fitted p_{ex} , we used the snow parameters from snowpits and soil parameters from the automatic sensors and fitted a scaling factor (pex_scaler) for measured p_{ex} profile and the unknown soil roughness (σ). pex_scaler varies from 0.8 to 1.8 with a step of 0.05, whereas σ varies from 0 to 5 mm with a step of 1 mm and varies from 0.1 to 0.5 cm with a step of 0.05 cm.

Fig. 8(a) shows that when the measured p_{ex} is high in one IOP, the MCMC-estimated p_{ex} is also high. However, Fig.8 (b) shows that within each IOP, the correlation between the measured p_{ex} and MCMC-estimated p_{ex} is low. Fig.8(c) shows the low correlation in (b) could be from the uncertainty in D_g observation and D_g - p_{ex} conversion equation; if p_{ex} is directly fitted from measured backscattering coefficient using the same radiative transfer model, it matches significantly better with the MCMC estimates. The result in Fig. 8(c) indicates BASE-AM is capable of estimating snow microstructure parameter together with the SD and SWE.

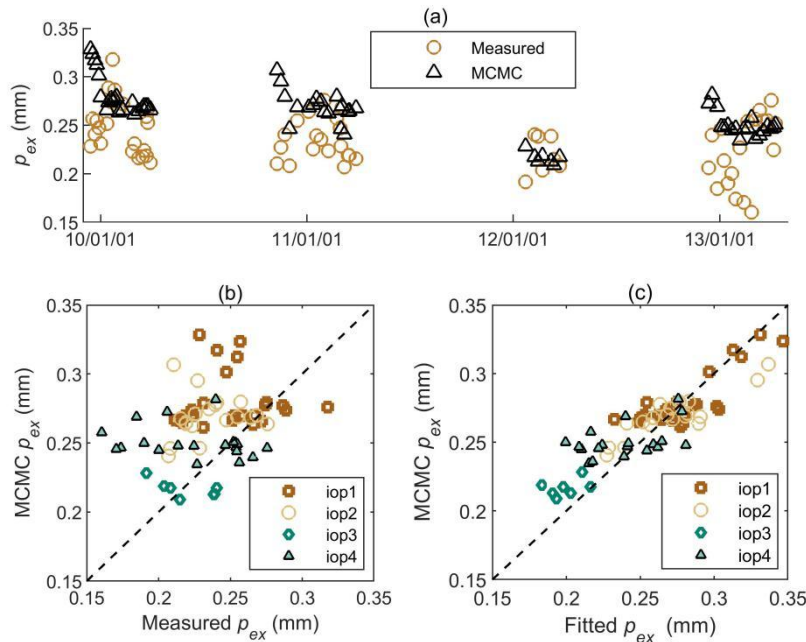


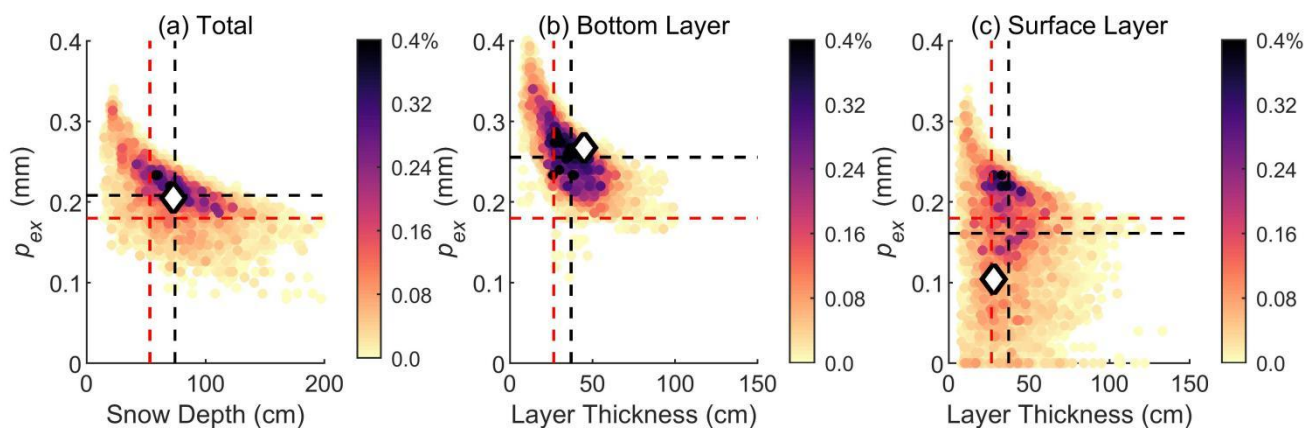
Figure 8: BASE-AM estimated profile-average exponential correlation length (p_{ex}) compared with the measured p_{ex} (p_{ex} converted from measured D_g) from snowpits in (a-b), and with the fitted p_{ex} in (c). The fitted p_{ex} comes from the use of MRMLS3&a to match the measured backscattering coefficient at three frequencies.

310

Fig. 9 uses 2-D distribution maps to show the relationship between layer thickness and exponential correlation length (p_{ex}) in the MCMC chains after the burn-in period, for Pit 49. After the burn-in period, all combinations of estimated variables can



reproduce the observation. Fig. 9 shows that the measured backscattering coefficients specify an up-down flipped logarithm-like relationship between layer thickness and p_{ex} : when layer thickness is high, p_{ex} is low, and vice versa; both parameters
 315 begin to saturate when the other approaches a high value. The area in dark purple is better represented in the MCMC chain, and thus has the highest probability, considering both observations and priors. This high probability area forms a logarithm-shape stripe instead of converging to a single point, reaffirming the importance of prior information in this retrieval problem. In Fig.9 (a) and (b), the observation changes the priors of layer thickness and p_{ex} at the cross of red dash lines to the posteriors at the cross of black dash lines. In general, there is more uncertainty in estimates of the surface-layer p_{ex} , than for
 320 the bottom-layer, because the sensitivity of radar backscatter to volume scattering decreases with decreasing p_{ex} .



325 **Figure 9:** 2D histogram of probability between layer thickness and exponential correlation length (p_{ex}) from the MCMC chain after burn-in period for Pit49: (a) for the entire snowpit, where the snow depth and mass-weighted average p_{ex} are presented, (b) for the bottom layer, (c) for the surface layer. The red dash lines represent the means of priors. The black dash lines represent the means of posteriors, which are the MCMC retrieval results. The white-face diamonds represent the measured layer thickness and p_{ex} converted from the measured D_g from the snowpit measurements.

5 Discussion

5.1 Concerning snow density, soil roughness and soil moisture

Backscattering coefficient at 10.2 GHz ($\sigma_{0,10.2}^{VV}$) is determined by snow density, soil liquid water content, and soil roughness,
 330 and we have shown the sensitivity of $\sigma_{0,10.2}^{VV}$ to the first two variables in Fig. 1. However, for each snowpit, a single observation of $\sigma_{0,10.2}^{VV}$ is insufficient to determine three variables. From our retrieval result, we found that regardless of the measured snow density (ranging from 150 to 300 kg/m³ over the dataset), the BASE-AM algorithm consistently estimated snow density to be approximately 215.5 kg/m³, with a standard deviation of only 7.0 kg/m³ across all snowpits. According to our simulations, the sensitivity of the microwave signal to snow density is lower than the soil parameters.
 335 This indicates that snow density is difficult to retrieve based on the current observations unless soil liquid water content and soil roughness are provided.



As to the other two soil variables, the results in Section 4 are based on the default BASE-AM algorithm configuration to estimate total soil water content and soil roughness simultaneously. To further explore the algorithm, we conducted an additional experiment estimating only the soil moisture, using a fixed soil roughness of 1 mm. We found that when both the two soil parameters were estimated, the simulated backscattering coefficient in MCMC is closer to the observations, which is 0.43 dB RMSE compared with 0.52 dB; in addition, the accuracy of MCMC-estimated SD and SWE is also slightly higher, with RMSEs for all snowpits as 10.2 cm and 28.67 mm, respectively, compared with 10.71 cm and 30.14 mm, respectively. However, Fig. 10 shows, when the soil roughness is fixed, the temporal variation of estimated soil liquid water content matches better with the sensor measurements, which means the soil liquid water content becomes retrievable. This suggests a possible strategy where the soil roughness is estimated at a single point early in the season, and the result used for the rest of the period if there is a desire to better estimate soil moisture dynamics from the radar data.

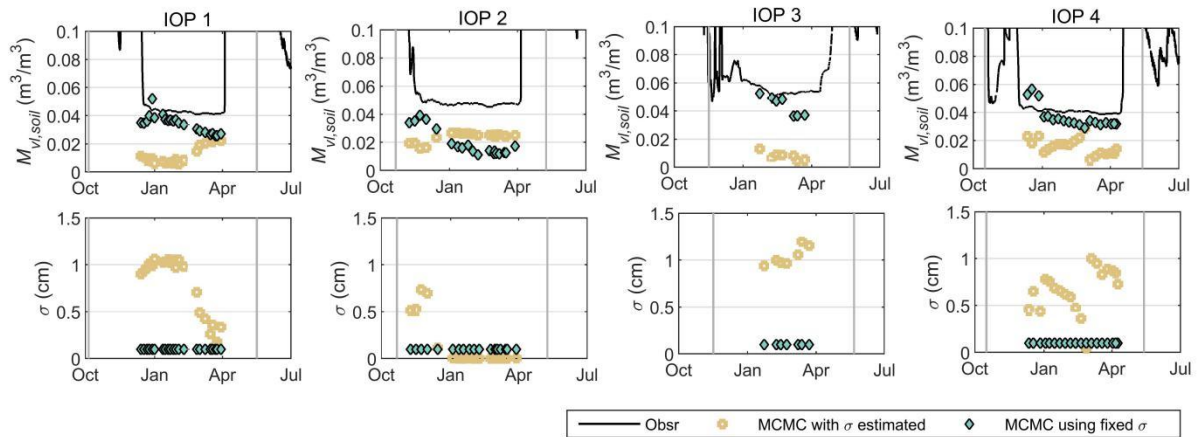


Figure 10: Comparison of MCMC-estimated soil liquid water content ($m_{vl,soil}$) and soil roughness (σ) when both soil moisture and soil roughness are estimated (light brown circles) or only the soil moisture is estimated (green diamonds). The MCMC $m_{vl,soil}$ is calculated from the MCMC-estimated total soil water content and soil temperature using the same unfrozen soil content module in the forward model.

5.2 The influence of the number of modeled snow layers on the retrieval

Fig. 11 shows the MCMC-estimated SD and SWE when the snow is assumed to have a single layer. The same snow and soil priors were used. When the one-layer snow assumption is used, BASE-AM cannot fully correct the underestimation of SWE prior. Fig. 12 show the MCMC-estimated p_{ex} is correlated with the fitted p_{ex} , but it has an overestimation. As summarized in Table 2, the snow retrieval result using two-layer assumption has a lower mean bias and lower RMSE. The one-layer assumption underestimates SD and SWE and overestimates profile-average p_{ex} .

Fig. 13 makes a comparison of the SD- p_{ex} relationship in MCMC chains determined by the same backscattering measurements for Pit49 using different snow layer assumptions. For the one-layer retrievals, the same three-frequency backscattering coefficients determined higher profile-average p_{ex} . Thus, the snow layer assumption can influence the SD and



p_{ex} estimation results, despite the priors utilized. At the same time, Fig. 13 agrees with the common sense that when more variables are estimated, the uncertainty of the variables increases.

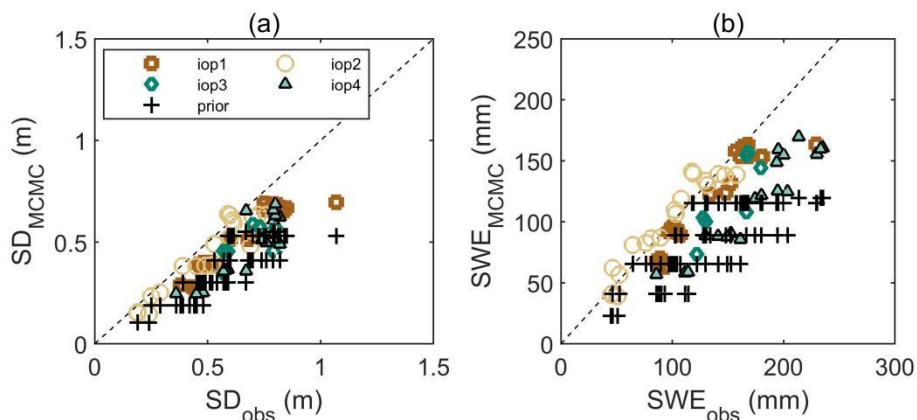


Figure 11: BASE-AM estimated snow depth (SD) (a) and snow water equivalent (SWE) (b) using one-layer snow assumption compared with the measurements.

365

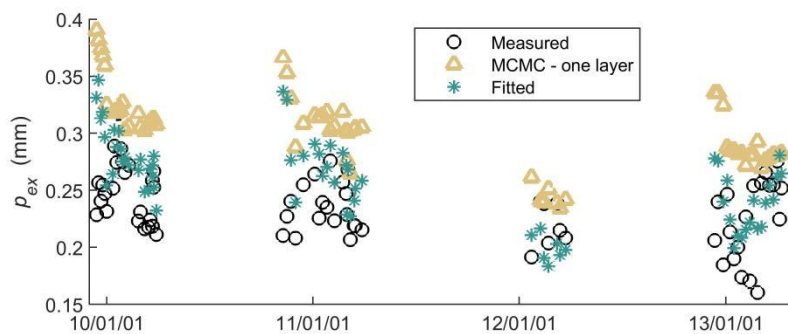
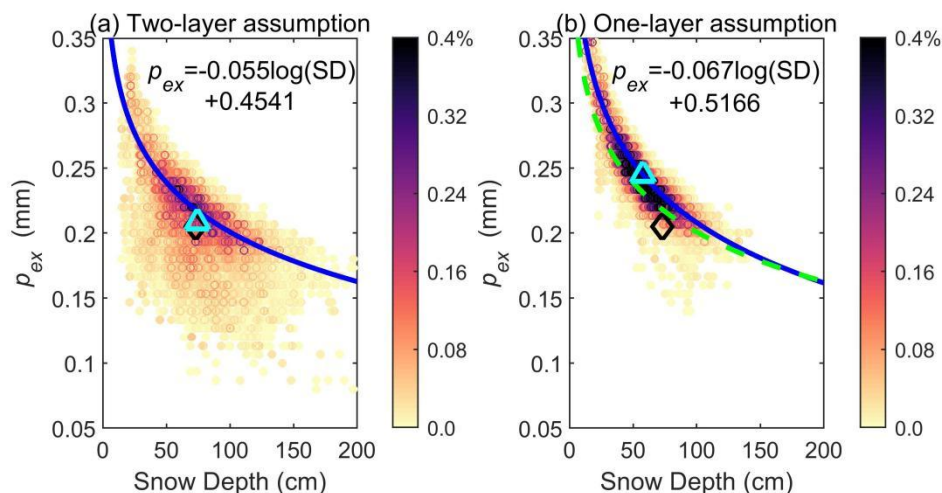


Figure 12: BASE-AM estimated p_{ex} using one-layer snow assumption compared with the measurements.



370 **Figure 13: Comparison between the SD and profile-average p_{ex} relationships in MCMC chains using two-layer (a) and one-layer (b) snow assumptions, respectively for Pit 49. The area of highest probability is used to fit a logarithm equation between SD and p_{ex} , and labeled as blue curve in both figures. The equation fitted in (a) are labeled as green curve in (b) to make a comparison. The measurements are labeled in black diamonds; the MCMC-estimated SD and p_{ex} are labeled as light blue triangles in both subfigures.**

375

Table 2. Summary of SD, SWE and profile-average exponential correlation length (p_{ex}) estimation error using two-layer and one-layer snow assumptions

Parameters	Period	Mean bias			RMSE		
		Prior	Posterior using two-layer snow assumption	Posterior using one-layer snow assumption	Prior	Posterior using two-layer snow assumption	Posterior using one-layer snow assumption
SD (cm)	All	-22.3	2.4	-13.4	24.0	10.2	15.9
SWE (mm)	All	-51.6	0.25	-23.5	60.0	28.7	35.5
Profile-average p_{ex} (mm)*	All	-0.078	0.004	0.045	0.086	0.019	0.0483

*Note: To compare with the MCMC p_{ex} , here we used the fitted p_{ex} instead of the snowpit-measured p_{ex} as the reference; the source of fitted p_{ex} can be found in Section 4.3.

380 6 Conclusions

In this paper, we developed a Bayesian-based Algorithm for SWE Estimation for Active Microwave (BASE-AM) to retrieve the snow and soil parameters from a site in Sodankylä, Finland based on X- and dual-Ku VV-pol. backscattering coefficient using biased SWE prior and uninformative snow microstructure priors. Results show that by predetermining the snowpack to have two layers, SD can be retrieved with a RMSE of 10.2 cm in 0-1 m range, and
 385 SWE can be retrieved with a RMSE of 28.7 mm in 0-200 mm range. The radar backscattering observations can correct



the bias of SD prior from -22.3 cm to 2.4 cm using two-layer snow assumptions, but it can be only corrected to -13.4 cm if one-layer snow assumption is used. Results assuming a single layer are significantly less accurate, despite using the same priors.

By iteratively updating several snow and soil variables in the MCMC chain and comparing the prior and posterior distributions, we showed that the key variables required to be estimated in BASE-AM are layer thickness, layer microstructure parameter and soil liquid water content. The backscattering coefficients in snow and soil are not sensitive to temperature, and thus temperature can be replaced by priors from land surface models. Backscattering intensity at low frequency is sensitive to snow density, but density cannot be easily retrieved unless soil parameters have been determined. The polarization splitting parameter (Q) in MEMLS3&a can be fixed unless cross-pol. backscattering observations are introduced.

Overall, our results indicate that active remote sensing observations coupled with globally-available prior information and a two-layer retrieval scheme can support estimation of SWE.

Appendix. The soil dielectric constant model

The soil dielectric constant model utilized in this paper was developed from the Mironov et al. (2004) model and revised according to the soil dielectric constant measurement experiment conducted by Jinmei Pan using Agilent analyzer in China. An introduction of the experiment can be found in Wu et al.(2022). Here a brief introduction of this model is provided, with more details to be published. The measurements utilized to develop this model covers a wider soil texture than Wu et al.(2002), from loamy sand (77.27 % sand, 16.02 % silt, 6.71 % clay) to silty clay loam (17.49 % sand, 49.68 % silt, 32.82 % clay). The gravimetric soil water content of all samples varies from 3% to 60%, and the soil temperature varies from -30 to 20 °C. Soil dielectric constants were measured from 200 MHz to 20 GHz continuously at 200 MHz steps.

The real and imaginary part of the squared root of soil dielectric constants (ϵ_{soil}) are the refractive index (RI) (n) and the normalized attenuation coefficient (NAC) (κ).

$$n + i\kappa = \sqrt{\epsilon_{soil}} = \epsilon'_{soil} + i\epsilon''_{soil} \quad (5)$$

n and κ of thaw soil are modeled as (Mironov et al., 2004):

$$n_s = \begin{cases} n_d + (n_b - 1)W, & W \leq W_B \\ n_d + (n_b - 1)W_B + (n_u - 1)(W - W_B), & W \geq W_B \end{cases} \quad (6)$$

$$\kappa_s = \begin{cases} \kappa_d + \kappa_b W, & W \leq W_B \\ \kappa_d + \kappa_b W_B + \kappa_u (W - W_B), & W \geq W_B \end{cases} \quad (7)$$

where, the subscripts of n and κ , which include d , b , and u represent dry soil solids, bound water, and free water. In the soil-water system, a fraction of bound water adheres to soil solids, which has a different dielectric property compared with free water. The maximum allowable bound water content is denoted as W_B . If the total water content (W) is lower than W_B , then the model will only contain two components, as the first lines of equation (6) and (7); otherwise, it will contain three components.

n and κ of frozen soil are modeled as (Mironov et al., 2017):



$$n_s = \begin{cases} n_d + (n_b - 1)W, & W \leq W_B \\ n_d + (n_b - 1)W_B + (n_t - 1)(W - W_B), & W_B \leq W \leq W_U \\ n_d + (n_b - 1)W_B + (n_t - 1)(W_U - W_B) + (n_i - 1)(W - W_U), & W \geq W_U \end{cases} \quad (8)$$

$$\kappa_s = \begin{cases} \kappa_d + \kappa_b W, & W \leq W_B \\ \kappa_d + \kappa_b W_B + \kappa_t(W - W_B), & W_B \leq W \leq W_U \\ \kappa_d + \kappa_b W_B + \kappa_t(W_U - W_B) + \kappa_i(W - W_U), & W \geq W_U \end{cases} \quad (9)$$

where, the subscripts of n and κ , which include d , b , t and i represent dry soil solids, bound water, transient water, and ice. Soil solids and bound water have the same physical meanings for frozen soil and for thaw soil. When soil temperature decreases from above-zero °C to subzero °C, not all water will immediately freeze into ice. The total volumetric fraction of unfrozen water is called the unfrozen water content (W_U), which can be calculated as a function of temperature and clay fraction. We followed the setting in Mironov et al.(2017) that the bound water will not freeze, and the unfrozen soil water that exceeds the bound water is considered as the transient water.

The key of soil dielectric constant model is to model W_B , W_U , and n and κ for all components. We utilized the same W_B and the same n and κ for soil solids as a function of clay fraction in Mironov et al. (2004). n and κ of ice refer to the temperature-dependent equation utilized in MEMLS3&a.

The dielectric constants of water components can be modeled by Debye's equation as:

$$\varepsilon = \varepsilon_\infty + \frac{\varepsilon_0 - \varepsilon_\infty}{1 - i2\pi f\tau} + i \frac{\sigma}{2\pi f \varepsilon_r} \quad (10)$$

where, ε_∞ is the dielectric constant in the high-frequency limit, ε_0 is the static dielectric constant in low-frequency limit, f is frequency (Hz), τ is the relaxation time (s), σ is the effective conductivity (S/m), and ε_r is the dielectric constant for free space (8.854×10^{-12} F/m). Later, ε can be transferred to n and κ using equation (5).

For each component, it requires to determine ε_0 , ε_∞ , τ , and σ . We adapted some existing equations from Mironov et al. (2004) and Stogryn (1971), and fitted the remaining according to measurements. We utilized the samples with $W < W_B$ to fit temperature-dependent bound water parameters, and then iteratively fit W_u and transient water parameters using MCMC approach. Table 3 lists the details of water component models, and W_U was determined as:

$$W_B = \min(A \times |T|^B, W) \quad (11)$$

$$A = a_c C + a_{mv} W$$

$$B = b_c C + b_{mv} W$$

where, C is soil clay content (%), T is soil temperature (°C), $a_c=0.00306$, $a_{mv}=0.394$, $b_c=0.00582$, and $b_{mv}=-1.073$.

Table 3. Sources or equations of ε_0 , ε_∞ , τ , and σ for different soil water components

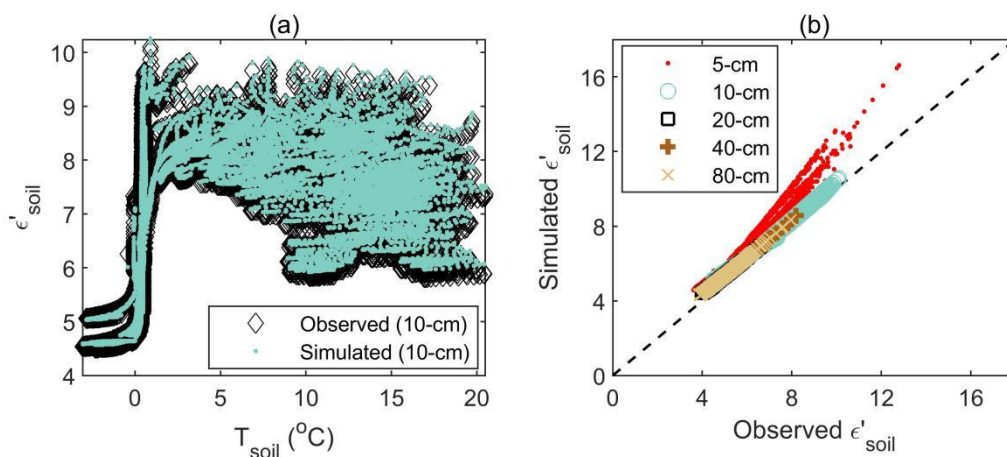
	ε_0	ε_∞	τ	σ
Free water	Stogryn (1971) as a function of T			Mironov et al. (2004) as a function of C
Bound water	$24.9 + 0.0685T$	$80.8 + 0.715T$	26.04×10^{-12}	Mironov et al. (2004) as a function of C



Transient water	4.78	77.90	24.0×10^{-12}	0.3913
-----------------	------	-------	------------------------	--------

* T and C are soil temperature ($^{\circ}\text{C}$) and soil clay content (%)

445 Fig. 14 shows an example of the model utilized to predict the measured soil permittivity (real part of dielectric constants) at 100 MHz by the Decagon 5 TM sensor in Sodankylä. The simulation utilized the measured liquid water content and measured soil texture. The total soil water content comes from the measured liquid water content before freezing. To calculate soil permittivity, we have used a fully-independent model compared to from the Decagon 5 TM sensor. Fig. 12(a) shows our model is capable of predicting the change of soil permittivity with soil temperature. Fig. 12(b) shows the simulated soil permittivity is highly consistent with the observations at 10 cm to 80 cm depth below the soil surface. The mean bias is 0.0838, with a RMSE of 0.0569. In addition, the model overestimates the measured permittivity for the single top layer at 5 cm, which is influenced by air above soil and organic matter. Including the 5-cm layer, the mean bias is 0.129 with a RMSE of 0.198. It indicates that the soil dielectric constant model described here is suitable to be used as part of the forward model in our paper.



455 **Figure 14: Simulated and observed real part of soil dielectric constants (ϵ'_{soil}) by Decagon 5 TM sensor at 100 MHz: (a) sensitivity to temperature for soil measured at 10 cm; (b) scatterplots for soil measured at different depths.**

460 **Data availability:** The NoSREx datasets are available after registration on the ESA Earth Observations Campaign Data portal (<https://earth.esa.int/web/guest/campaigns>).

465 **Author contribution:** JL provided the NoSREx datasets, and preliminary analysis of these datasets was conducted by JP, MD, and JL prior to retrieval. MD and DL provided the MCMC algorithm ideas and tools, which were later implemented and revised by JP to conduct the SWE retrieval experiments. All co-authors participated in the analysis of the MCMC results and collaborated on writing and revising the manuscript together.



Competing interests: The authors declare that they have no conflict of interest.

470 **Acknowledgment**

The authors want to thank the NoSREx team for their hard work and dedicated efforts for completing this snow experiment and providing the great dataset to support our study. We want to thank Kimmo Rautiainen for providing the soil frost depth measurement for us to do more analysis, and thank Simon Yueh and Richard Kelly for providing valuable comments when we were studying the first MCMC outputs. We dedicate this study to the memory of Dr. Joshua King, who tragically passed away February 21, 2023. Josh's pioneering measurements and keen insight into estimation of snow water equivalent from radar observations were an inspiration for us and for the entire community, and he will be deeply missed. This work was funded by the National Key Research and Development Program of China (Grant No. 2021YFB3900104), the National Natural Science Foundation of China (Grant No. 42090014), NASA grant 80NSSC17K0200, and was financially supported by the China Scholarship Council and the OSU Presidential Fellowship given to Jinmei Pan.

480 **References**

- Barnett, T. P., Adam, J. C., and Lettenmaier, D. P.: Potential impacts of a warming climate on water availability in snow-dominated regions, *Nature*, 438, 303–309, <https://doi.org/10.1038/nature04141>, 2005.
- Brown, R. D. and Robinson, D. A.: Northern Hemisphere spring snow cover variability and change over 1922–2010 including an assessment of uncertainty, *Cryosph.*, 5, 219–229, <https://doi.org/10.5194/tc-5-219-2011>, 2011.
- 485 Cline, D., Elder, K., Davis, R., Hardy, J., Liston, G., Imel, D., Yueh, S., Gasiewski, A., Koh, G., Armstrong, R., and Parsons, M.: Overview of the NASA cold land processes field experiment (CLPX-2002), *Proc SPIE*, 4894, <https://doi.org/10.1117/12.467766>, 2003.
- Cui, Y., Xiong, C., Lemmetyinen, J., Shi, J., Jiang, L., Peng, B., Li, H., Zhao, T., Ji, D., and Hu, T.: Estimating snow water equivalent with backscattering at X and Ku band based on absorption loss, *Remote Sens.*, 8, 505, <https://doi.org/10.3390/rs8060505>, 2016.
- 490 Derksen, C., King, J., Belair, S., Garnaud, C., Vionnet, V., Fortin, V., Lemmetyinen, J., Crevier, Y., Plourde, P., Lawrence, B., van Mierlo, H., Burbidge, G., and Siqueira, P.: Development of the Terrestrial Snow Mass Mission, in: 2021 IEEE International Geoscience and Remote Sensing Symposium IGARSS, Brussels, Belgium, 614 – 617, <https://doi.org/10.1109/IGARSS47720.2021.9553496>, 2021.
- 495 Durand, M., Barros, A., Dozier, J., Adler, R., Cooley, S., Entekhabi, D., Forman, B. A., Konings, A. G., Kustas, W. P., Lundquist, J. D., Pavelsky, T. M., Rodell, M., and Steele-Dunne, S.: Achieving Breakthroughs in Global Hydrologic Science



- by Unlocking the Power of Multisensor, Multidisciplinary Earth Observations, *AGU Adv.*, 2, e2021AV000455, <https://doi.org/https://doi.org/10.1029/2021AV000455>, 2021.
- 500 Flanner, M. G., Shell, K. M., Barlage, M., Perovich, D. K., and Tschudi, M. A.: Radiative forcing and albedo feedback from the Northern Hemisphere cryosphere between 1979 and 2008, *Nat. Geosci.*, 4, 151–155, <https://doi.org/10.1038/ngeo1062>, 2011.
- Gelman, A., Carlin, J.B., Stern, H.S., and Rubin, D.B.: Metropolis and metropolis-hasting algorithms, in: *Bayesian Data Analysis (2nd ed.)*, edited by: Gelman, A., Carlin, J.B., Stern, H.S., and Rubin, D.B., Chapman & Hall/CRC, Boca Raton, FL, USA, 320–334, <https://doi.org/10.1201/9780429258480>, 2003.
- 505 Integrated Global Observing Strategy (IGOS): IGOS cryosphere theme : a cryosphere theme report for the IGOS partnership. WMO/TD-No. 1405, Geneva, Switzerland, 114 pp., 2007.
- Jordan, R.: A One-Dimensional Temperature Model for a Snow Cover: Technical Documentation for SN THERM.89, U.S. Army Corps of Engineers, Cold Regions Research & Engineering Laboratory, 1991.
- 510 King, J., Derksen, C., Toose, P., Langlois, A., Larsen, C., Lemmetyinen, J., Marsh, P., Montpetit, B., Roy, A., Rutter, N., and Sturm, M.: The influence of snow microstructure on dual-frequency radar measurements in a tundra environment, *Remote Sens. Environ.*, 215, 242–254, <https://doi.org/10.1016/j.rse.2018.05.028>, 2018.
- Lemmetyinen, J., Kontu, A., Pulliainen, J., Vehviläinen, J., Rautiainen, K., Wiesmann, A., Mätzler, C., Werner, C., Rott, H., Nagler, T., Schneebeli, M., Proksch, M., Schüttemeyer, D., Kern, M., and Davidson, M. W. J.: Nordic Snow Radar Experiment, *Geosci. Instrumentation, Methods Data Syst.*, <https://doi.org/10.5194/gi-5-403-2016>, 2016.
- 515 Lemmetyinen, J., Ruiz, J. J., Cohen, J., Haapamaa, J., Kontu, A., Pulliainen, J., and Praks, J.: Attenuation of Radar Signal by a Boreal Forest Canopy in Winter, *IEEE Geosci. Remote Sens. Lett.*, 19, 1–5, <https://doi.org/10.1109/LGRS.2022.3187295>, 2022.
- Lettenmaier, D. P., Alsdorf, D., Dozier, J., Huffman, G. J., Pan, M., and Wood, E. F.: Inroads of remote sensing into hydrologic science during the WRR era, *Water Resour. Res.*, 51, 7309 – 7342, <https://doi.org/https://doi.org/10.1002/2015WR017616>, 2015.
- 520 Macelloni, G., Brogioni, M., Montomoli, F., and Fontanelli, G.: Effect of forests on the retrieval of snow parameters from backscatter measurements, *Eur. J. Remote Sens.*, 45, 121–132, <https://doi.org/10.5721/EuJRS20124512>, 2012.
- Mätzler, C.: Relation between grain-size and correlation length of snow, *J. Glaciol.*, <https://doi.org/10.3189/172756502781831287>, 2002.
- 525 Merkouriadi, I., Lemmetyinen, J., Liston, G. E., and Pulliainen, J.: Solving Challenges of Assimilating Microwave Remote Sensing Signatures With a Physical Model to Estimate Snow Water Equivalent, *Water Resour. Res.*, 57, 1 – 24, <https://doi.org/10.1029/2021WR030119>, 2021.
- Mironov, V. L., Dobson, M. C., Kaupp, V. H., Komarov, S. A., and Kleshchenko, V. N.: Generalized refractive mixing dielectric model for moist soils, *IEEE Trans. Geosci. Remote Sens.*, 42, 773 – 785, <https://doi.org/10.1109/TGRS.2003.823288>, 2004.
- 530



- Mironov, V. L., Kosolapova, L. G., Lukin, Y. I., Karavaysky, A. Y., and Molostov, I. P.: Temperature- and texture-dependent dielectric model for frozen and thawed mineral soils at a frequency of 1.4 GHz, *Remote Sens. Environ.*, 200, 240–249, <https://doi.org/10.1016/j.rse.2017.08.007>, 2017.
- 535 Mortimer, C., Mudryk, L., Derksen, C., Luoju, K., Brown, R., Kelly, R., and Tedesco, M.: Evaluation of long-term Northern Hemisphere snow water equivalent products, *Cryosph.*, 14, 1579–1594, <https://doi.org/10.5194/tc-14-1579-2020>, 2020.
- Montpetit, B., Royer, A., Wigneron, J. P., Chanzy, A., and Mialon, A.: Evaluation of multi-frequency bare soil microwave reflectivity models, *Remote Sens. Environ.*, 162, 186–195, <https://doi.org/10.1016/j.rse.2015.02.015>, 2015.
- 540 Pan, J., Durand, M. T., Vander Jagt, B. J., and Liu, D.: Application of a Markov Chain Monte Carlo algorithm for snow water equivalent retrieval from passive microwave measurements, *Remote Sens. Environ.*, 192, 150 – 165, <https://doi.org/10.1016/j.rse.2017.02.006>, 2017.
- Picard, G., Löwe, H., Domine, F., Arnaud, L., Larue, F., Favier, V., Le Meur, E., Lefebvre, E., Savarino, J., and Royer, A.: The Microwave Snow Grain Size: A New Concept to Predict Satellite Observations Over Snow-Covered Regions, *AGU Adv.*, 3, e2021AV000630, <https://doi.org/https://doi.org/10.1029/2021AV000630>, 2022.
- 545 Proksch, M., Mätzler, C., Wiesmann, A., Lemmetyinen, J., Schwank, M., Löwe, H., and Schneebeli, M.: MEMLS3&a: Microwave Emission Model of Layered Snowpacks adapted to include backscattering, *Geosci. Model Dev.*, 8, 2611–2626, <https://doi.org/10.5194/gmd-8-2611-2015>, 2015.
- Rincon, R., Osmanoglu, B., Racette, P., Perrine, M., Brucker, L., Seufert, S., Kielbasa, C., and Warren, A.: Performance of Swesarr’ s Multi-Frequency Dual-Polarimetry Synthetic Aperture Radar During Nasa’ S Snowex Airborne Campaign, in: 550 2020 IEEE International Geoscience and Remote Sensing Symposium, Waikoloa, HI, USA, 6150–6153, <https://doi.org/10.1109/IGARSS39084.2020.9324391>, 2020.
- Rott, H., Duguay, C., Etchevers, P., Essery, R., Hajnsek I., Macelloni, G., Malnes, E., and Pulliainen, J.: Report for Mission Selection: CoReH20, ESA SP-1324/2, ESA Communications, Noordwijk, The Netherlands, 192 pp., 2012.
- 555 Rutter, N., Sandells, M. J., Derksen, C., King, J., Toose, P., Wake, L., Watts, T., Essery, R., Roy, A., Royer, A., Marsh, P., Larsen, C., and Sturm, M.: Effect of snow microstructure variability on Ku-band radar snow water equivalent retrievals, *The Cryosphere*, 13, 3045–3059, <https://doi.org/10.5194/tc-13-3045-2019>, 2019.
- Shi, J., Dong, X., Zhao, T., Du, J., Jiang, L., Du, Y., Liu, H., Wang, Z., Ji, D., and Xiong, C.: WCOM: The science scenario and objectives of a global water cycle observation mission, in: 2014 IEEE Geoscience and Remote Sensing Symposium, Quebec City, QC, Canada, 3646–3649, <https://doi.org/10.1109/IGARSS.2014.6947273>, 2014.
- 560 Takala, M., Luoju, K., Pulliainen, J., Derksen, C., Lemmetyinen, J., Kärnä, J. P., Koskinen, J., and Bojkov, B.: Estimating northern hemisphere snow water equivalent for climate research through assimilation of space-borne radiometer data and ground-based measurements, *Remote Sens. Environ.*, <https://doi.org/10.1016/j.rse.2011.08.014>, 2011.
- Tsang, L., Durand, M., Derksen, C., Barros, A. P., Kang, D.-H., Lievens, H., Marshall, H.-P., Zhu, J., Johnson, J., King, J., Lemmetyinen, J., Sandells, M., Rutter, N., Siqueira, P., Nolin, A., Osmanoglu, B., Vuyovich, C., Kim, E., Taylor, D.,



- 565 Merkouriadi, I., Brucker, L., Navari, M., Dumont, M., Kelly, R., Kim, R. S., Liao, T.-H., Borah, F., and Xu, X.: Review article: Global monitoring of snow water equivalent using high-frequency radar remote sensing, *Cryosph.*, 16, 3531–3573, <https://doi.org/10.5194/tc-16-3531-2022>, 2022.
- Wu, S., Zhao, T., Pan, J., Xue, H., Zhao, L., and Shi, J.: Improvement in Modeling Soil Dielectric Properties During Freeze-Thaw Transitions, *IEEE Geosci. Remote Sens. Lett.*, 19, 1–5, <https://doi.org/10.1109/LGRS.2022.3154291>, 2022.
- 570 Xu, X., Liang, D., Tsang, L., Andreadis, K. M., Josberger, E. G., Lettenmaier, D. P., Cline, D. W., and Yueh, S. H.: Active Remote Sensing of Snow Using NMM3D/DMRT and Comparison With CLPX II Airborne Data, *IEEE J. Sel. Top. Appl. Earth Obs. Remote Sens.*, 3, 689–697, <https://doi.org/10.1109/JSTARS.2010.2053919>, 2010.
- Zhu, J., Tan, S., King, J., Derksen, C., Lemmetyinen, J., and Tsang, L.: Forward and Inverse Radar Modeling of Terrestrial Snow Using SnowSAR Data, *IEEE Trans. Geosci. Remote Sens.*, 56, 7122 – 7132, <https://doi.org/10.1109/TGRS.2018.2848642>, 2018.
- 575 Zhu, J., Tan, S., Tsang, L., Kang, D., and Kim, E. : Snow Water Equivalent Retrieval Using Active and Passive Microwave Observations, *Water Resour. Res.*, 57(7), <https://doi.org/10.1029/2020wr027563>, 2021.